

## OCEANOGRAPHY

# Pathways and modification of warm water flowing beneath Thwaites Ice Shelf, West Antarctica

A. K. Wåhlin<sup>1\*</sup>, A. G. C. Graham<sup>2</sup>, K. A. Hogan<sup>3</sup>, B. Y. Queste<sup>1</sup>, L. Boehme<sup>4</sup>, R. D. Larter<sup>3</sup>, E. C. Pettit<sup>5</sup>, J. Wellner<sup>6</sup>, K. J. Heywood<sup>7</sup>

Thwaites Glacier is the most rapidly changing outlet of the West Antarctic Ice Sheet and adds large uncertainty to 21st century sea-level rise predictions. Here, we present the first direct observations of ocean temperature, salinity, and oxygen beneath Thwaites Ice Shelf front, collected by an autonomous underwater vehicle. On the basis of these data, pathways and modification of water flowing into the cavity are identified. Deep water underneath the central ice shelf derives from a previously underestimated eastern branch of warm water entering the cavity from Pine Island Bay. Inflow of warm and outflow of melt-enriched waters are identified in two seafloor troughs to the north. Spatial property gradients highlight a previously unknown convergence zone in one trough, where different water masses meet and mix. Our observations show warm water impinging from all sides on pinning points critical to ice-shelf stability, a scenario that may lead to unpinning and retreat.

## INTRODUCTION

Satellite-borne altimetry and interferometry data show large spatial variation in melt rates and grounding-zone retreat for Thwaites Ice Shelf. Locally, melt rates can exceed 10 times (1) the ice-shelf average value of  $\sim 17.7$  m/year (2). Large variations have also been observed in other ice shelves (3) and are attributed to interactions of oceanic processes with seafloor topography underneath the floating ice (4). However, to date, no measurements of water masses beneath Thwaites Ice Shelf have been conducted, and only very few surveys exist near the ice-shelf fronts (5, 6); therefore, fundamental properties of the ocean circulation beneath it are still unknown. Specifically, it is not yet clear where the main entry points for warm water are, how far into the cavity the warm water penetrates, or how the rate of ice melting relates to the warm water inflow.

The Thwaites Ice Shelf consists of the faster flowing Thwaites Glacier Tongue and the slower flowing Eastern Ice Shelf (Fig. 1). Direct observations of water depth are lacking in the coastal vicinity and ice-shelf cavity; therefore, all studies so far have used estimates of bathymetry derived from inversions of airborne gravity survey data (7, 8). These inversions predict the existence of three deep troughs at the northern ice front (“T1”, “T2”, and “T3” in Fig. 1), which are hypothesized, in turn, to direct warm dense water into the cavity, potentially accessing the base of the ice shelf and grounding zones. These troughs branch from a 1300-m-deep northern basin (Thwaites Trough) that connects to Pine Island Trough further north along the continental shelf. This northern front of the Thwaites Ice Shelf provides access to the main deep basin at the grounding zone, but there is also an eastern-facing front that provides access to

a more eastern deep basin, separated from the main basin by a submarine ridge (Fig. 1). This basin beneath the Eastern Ice Shelf extends eastward to a 1400-m-deep area, partially separated from Pine Island Trough by an irregular ridge (Fig. 1).

Ship-based conductivity-temperature-depth (CTD) transects (fig. S2) (5, 6) from the eastern front show that the deep water (800 to 1300 m) in the eastern basin is warm (conservative temperature  $\theta = 1.1$  to  $1.2^\circ\text{C}$ ) (9), salty (absolute salinity  $S_A = 34.85$  to  $34.87$  g/kg) (9), and weakly stratified. In Thwaites Trough, the deep water is more well mixed (more uniform) with  $S_A = 34.885$  g/kg and  $\theta = 1.13^\circ$  to  $1.15^\circ\text{C}$  (2014) and  $\theta = 1.15^\circ$  to  $1.20^\circ\text{C}$  (2010). The higher salinity in Thwaites Trough indicates that it receives a deeper type of Circumpolar Deep Water (CDW) (10), which is possible since it has a greater sill depth than the eastern part of Pine Island Trough (8). The variability in deep water temperatures is larger in the eastern basin than in the northern (temporal variation as well as vertical and horizontal; fig. S2), reflecting that temperature varies substantially in time and space in Pine Island Trough due to local and cross-shelf forcing (11, 12). This variability ultimately originates from the source water, Lower Circumpolar Deep Water (LCDW), which, outside the continental shelf at 600 to 800 m in depth, has a temperature range of  $0.95^\circ$  to  $1.5^\circ\text{C}$  but a narrow salinity range of 34.895 to 34.905 g/kg (10, 13–15). The highest concentration of meltwater is found in Thwaites Trough, with temperature and salinity near the meltwater mixing line (or “Gade line”; fig. S2A) (16, 17). Stations further east contain mixtures of CDW and Winter Water (WW) (WW; fig. S2A) (18).

Up to now, there have been no data defining the circulation of warm water into and under the Thwaites Ice Shelf. Thus, it remains unclear through which deep channel water flows into the cavity and what pathways the water takes underneath the ice shelf. The gravity-derived bathymetry suggests that a ridge blocks access to deeper parts of the subglacial basin (Fig. 1) from the east, whereas warm water may enter beneath the Thwaites Glacier Tongue from the north along the deep troughs. Model results indicate that Thwaites Glacier retreat is linked to the dynamics of the ocean (19, 20), that the main pathways for warm water are from the north (20), and that the comparatively small volume of deep water entering from the eastern ice front only makes it a few kilometers underneath the ice

<sup>1</sup>Department of Marine Sciences, University of Gothenburg, Box 461, 405 30 Gothenburg, Sweden. <sup>2</sup>College of Marine Science, University of South Florida, St. Petersburg, FL 33701, USA. <sup>3</sup>British Antarctic Survey, High Cross, Madingley Road, Cambridge CB3 0ET, UK. <sup>4</sup>Scottish Oceans Institute, University of St Andrews, East Sands, St. Andrews, Fife, UK. <sup>5</sup>College of Earth, Ocean, and Atmospheric Sciences, Oregon State University, Weniger Hall 533, 103 SW Memorial Place, Corvallis, OR 97331, USA. <sup>6</sup>Department of Earth and Atmospheric Sciences, University of Houston, Houston, TX 77204-5007, USA. <sup>7</sup>Centre for Ocean and Atmospheric Sciences, School of Environmental Sciences, University of East Anglia, Norwich, UK.

\*Corresponding author. Email: awahlin@gu.se

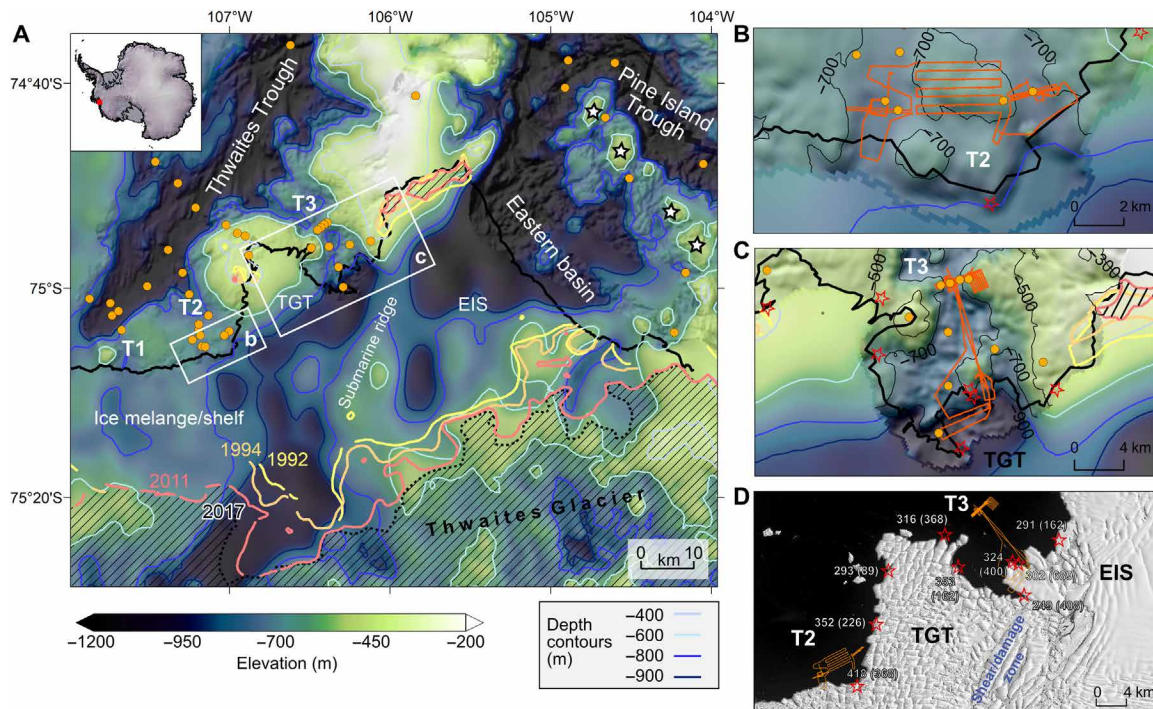


**Fig. 1. Maps of the survey region showing the Thwaites Glacier Tongue and Eastern Ice Shelf.** Colors indicate bathymetry according to color bar, unsurveyed areas appear smoother as bathymetry from gravity inversion (7) is shown, and black solid line shows ice shelf and melange front in mid-February 2019. Orange dots indicate conductivity-temperature-depth (CTD) cast locations. (A) Bathymetry with notations indicating bathymetric features and areas discussed in the main text. Hatched regions show grounded ice, and colored lines show grounding line positions in the years indicated (1, 26) and the pinning point for Eastern Ice Shelf near the center of (A). White boxes outline areas shown in detail in (B) and (C), and orange lines in (B) to (D) show the autonomous underwater vehicle (AUV) mission paths. White stars indicate the irregular ridge separating Pine Island Bay from the eastern basin discussed in the text. (D) Ice-shelf front mapped with the multibeam echosounder overlaid on a grayscale Landsat 8 image of Thwaites ice front from 13 February 2019. The shear zone marking the boundary between Eastern Ice Shelf (EIS) and Thwaites Glacier Tongue (TGT) is indicated by blue text. Red stars mark the segments where average ice-shelf depths below sea level were calculated; numbers are the average ice-shelf face depths for that segment (see Methods), and numbers in parentheses are water column thickness (i.e., depth minus ice-shelf draft).

shelf (20). However, model outputs are poorly constrained because of the paucity of observations. Key results and boundary conditions such as bathymetry, water pathways, flow rates, and temperatures need to be validated by observations to improve predictions.

## RESULTS

To address these critical knowledge gaps, cruise NBP19-02 collected oceanographic and geophysical observations in the Amundsen Sea embayment in February to March 2019. Favorable ice and weather conditions provided an unprecedented opportunity to access uncharted regions of the central and western parts of Thwaites Ice Shelf front. The draft of the northward-facing ice front was estimated to be between 291 and 418 m (Fig. 1D and see Methods), confirming that the base of ice at the northern tip of the Thwaites Glacier Tongue is close to the seafloor, if not still in contact with it, and that the front is highly irregular. A new detailed coastal bathymetry, acquired using a hull-mounted multibeam echo sounder, confirmed the presence of troughs that lead in toward the ice shelf either side of the Thwaites Glacier Tongue (Fig. 1 and see Methods). These troughs are notably deeper (by 100 to 300 m) than predicted by gravity models (8, 21). Temperature, salinity, oxygen content, and current velocity were measured in these troughs by ship-borne instrumentation and an autonomous underwater vehicle (AUV). The AUV, a Kongsberg “Hugin” depth-rated to 3000 m, was equipped

with instrumentation to measure hydrographic and chemical properties of the water in situ (see Methods). It was deployed in two of the three deep troughs that lead from Thwaites Trough to the central part of the ice shelf and part way under it (Figs. 1 and 2). The AUV followed a path at an altitude of 50 m above the seafloor for most of the missions, except on cross-trough transects where it was operated at a range of different (constant) depths (figs. S3 and S4). Warm water (up to  $\theta = 0.8^\circ$  to  $1.05^\circ\text{C}$ ) was observed at the bottom of both troughs (Fig. 2 and fig. S3). The thickness of the warm water layer was between 200 and 300 m (figs. S3 to S5), with the  $0^\circ$  isotherm at about 500 m in depth. In trough T2, data collected with the ship’s hull-mounted acoustic Doppler current profiler (ADCP) system show a northward outflow of water above 500 m (see Fig. 2, Methods, and fig. S5), while in trough T3 (Fig. 1), there is southward flow at all depths transporting warm water toward the ice-shelf cavity (Fig. 2 and fig. S5). The southward heat transport in trough T3 alone was estimated as 0.9 TW, which corresponds to melting 85 Gt/year glacial ice (see Methods). This estimate is describing what is transported into the cavity in only one of the three inflow sites that have been identified here, and it is not known how much of the available energy that is used to melt ice once inside the cavity. However, the fact that the number is similar to the basal melt for the entire ice shelf (97.5 Gt/year) over the period 2010–2018 as estimated from satellite altimetry (3) indicates that the inflow in T3 is likely impacting the basal melt of the entire system.

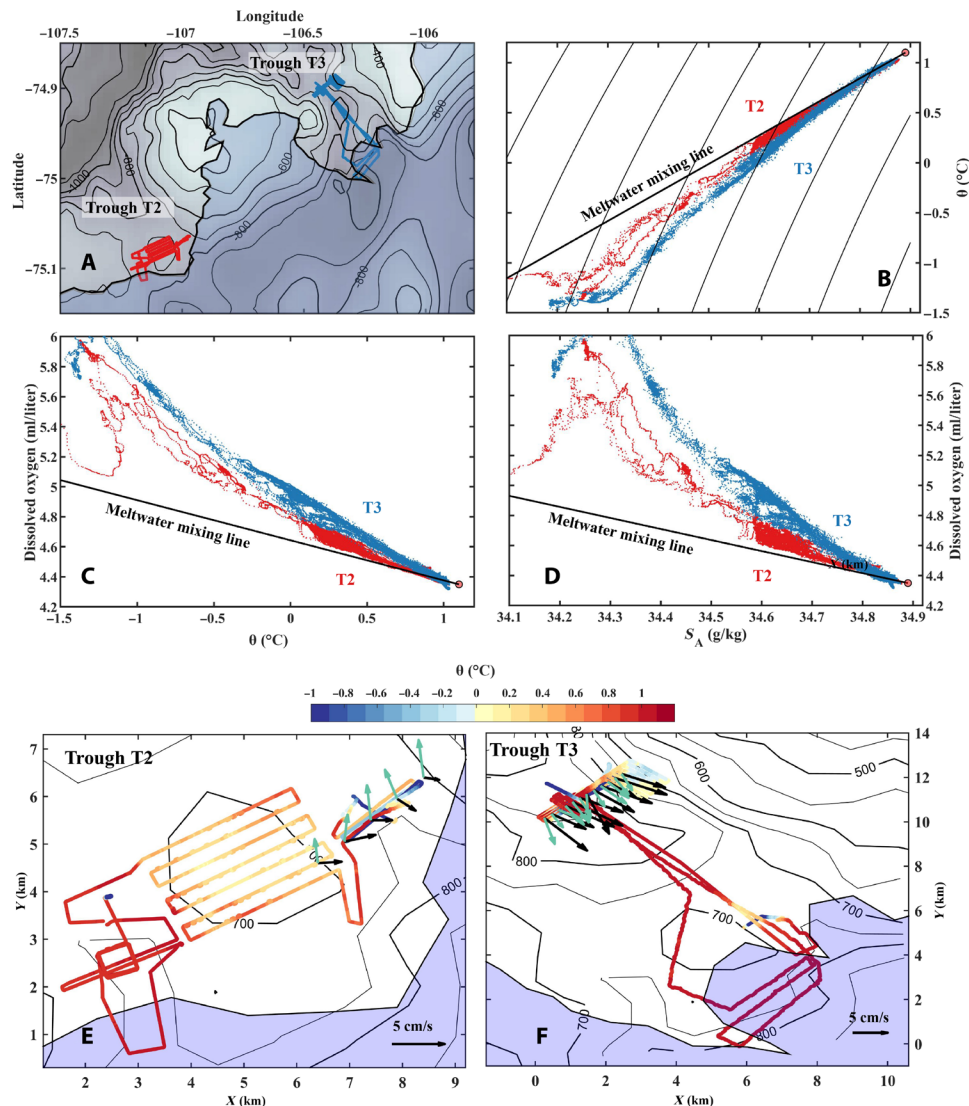


**Fig. 2. Data from troughs T2 and T3 (Fig. 1).** (A) Mission tracks for both troughs. (B) Conservative temperature  $\theta$  (in degrees Celsius) versus absolute salinity  $S_A$  (in grams per kilogram), colors as in (A). Black contours are potential density. (C) Dissolved oxygen (in milliliters per liter) versus conservative temperature  $\theta$  (in degrees Celsius). (D) Dissolved oxygen (in milliliters per liter) versus absolute salinity (in grams per kilogram). Black lines in (B) to (D) are the mixing lines between CDW (red circle) and glacial melt (see Methods) (16–18). (E and F) Conservative temperature  $\theta$  (color bar) along the AUV track together with detided current velocity from the ship's hull-mounted ADCP. Green arrows are average current velocity for a depth of 0 to 400 m, and black arrows are average current velocity for a depth of >400 m. For raw data, see fig. S5. Black arrow in lower right corner is scale arrow (5 cm/s). Ice shelf is indicated by blue transparent area, and depth contours are every 50 m. (E) Trough T2. (F) Trough T3. Note that most of the temperature variation in (E) and (F) are due to depth variations (see fig. S4 for depth and salinity along the AUV path)

When warm salty ocean water comes in contact with and melts glacial ice, it becomes colder [due to loss of latent heat and cooling by the ice (16)], fresher (due to the mixing with meltwater), and more oxygenated [due to high levels of dissolved oxygen in the meltwater (17, 18)]. This information is used in Fig. 2 to reveal that in trough T2, throughout the water column, the concentration of meltwater was consistently higher compared with that in trough T3. The flow direction is southward for all depths in trough T3, but in T2, the flow appears to switch direction: It is northward from the surface to about 400 m, but there is a vertical shear and near-zero or even negative (i.e., southward) velocities near the edge of the ADCP range (fig. S5). The northward outflow near the surface in trough T2 has the highest meltwater content (Fig. 2), which is seen more

clearly in Fig. 3 where the ship-borne CTD data (including near-surface waters) are plotted together with the AUV data. The westernmost parts of Thwaites Trough have water that is nearly saturated with meltwater [i.e., contact with glacial ice (22) has cooled the water to near-surface freezing temperature (marked by blue arrows)]. This shows that the meltwater produced by Thwaites is exiting in the west, in agreement with model results (20, 23). Near-bottom water encountered by the AUV in trough T2 has temperature-salinity-oxygen properties similar to deep water in Thwaites Trough and higher influence of glacial melt, while in trough T3, there are no traces of glacial melt. Near-bottom water in trough T3 is similar to that found in Thwaites Trough, but deep water resembling that in Pine Island Bay is also present (Fig. 4).

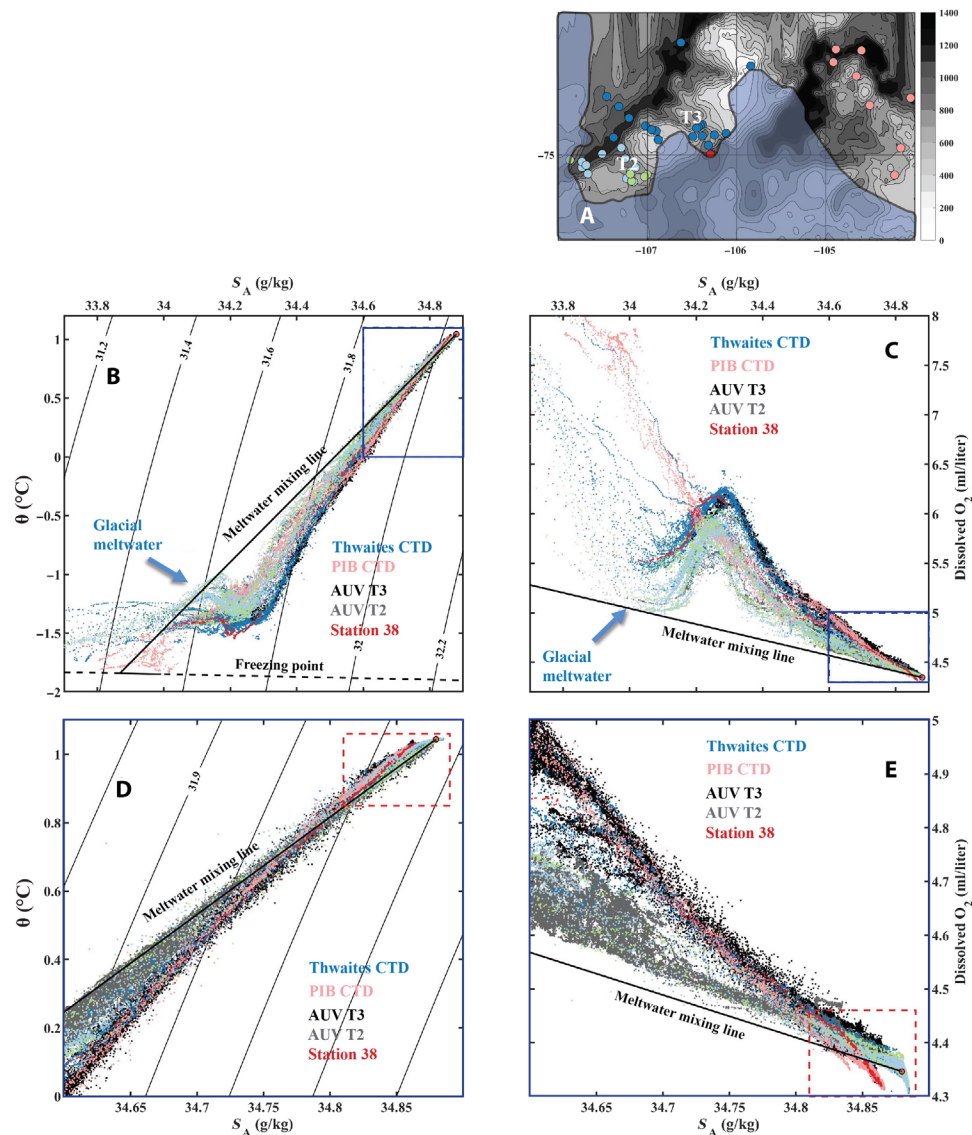


**Fig. 3. Visualization of different water masses in the surveyed area.** Hydrographic data obtained by CTD [colors correspond to stations in (A)]. Pine Island Bay is indicated by PIB together with data obtained by the AUV (black is the mission in trough T3, and gray is the mission in trough T2). Solid black line shows the mixing line between CDW and ice shelf melt (see Methods) (16, 18, 40). (A) Map of the region. (B) Conservative temperature  $\theta$  (in degrees Celsius) versus absolute salinity  $S_A$  (in grams per kilogram). Dashed black line shows the freezing point at surface pressure (9), and solid contours show the potential density. (C) Dissolved oxygen (in milliliters per liter) versus absolute salinity  $S_A$  (in grams per kilogram). (D) Conservative temperature  $\theta$  (in degrees Celsius) versus absolute salinity  $S_A$  (in grams per kilogram) for the zoomed parameter space indicated by blue box in (B). Solid contours show the potential density. (E) Dissolved oxygen (in milliliters per liter) versus absolute salinity  $S_A$  (in grams per kilogram) for the zoomed parameter space indicated by blue box in (C). Blue arrows in (B) and (C) indicate the high meltwater concentrations discussed in the main text.

As the vehicle traveled along the seabed in trough T3, water of comparatively low salinity ( $S_A = 34.865$  g/kg) and conservative temperature  $\theta$  between  $1.03^\circ$  and  $1.04^\circ\text{C}$  was encountered at 1050 m depth underneath the ice shelf (Figs. 4 and 5). The fresher deep water type was also observed at CTD station 38 (Fig. 4), a station very near the ice-shelf front and overlapping with the AUV path, and in Pine Island Bay, consistent with historical data (fig. S2). These observations show that deep water originating in Pine Island Bay has traveled beneath the Eastern Ice Shelf to reach trough T3. This water mass is hence extending significantly further west than previously expected and suggested in modeling (20). This indicates that the bathymetric ridge underneath Eastern Ice Shelf (Fig. 1) is either

deeper than 1050 m, in contrast to  $\sim 700$  to 800 m obtained by gravity inversion (7, 8), or does not extend far enough north to block the Pine Island Bay deep water. Since the AUV mission in trough T2 only went 600 m into the cavity (compared to 3 km for trough T3) and only to 800 m in depth (compared to 1050 m for trough T3), we do not know the western extent of the Pine Island Bay water. It might reside at greater depths or further into the cavity also west of the shear zone.

Figure 5 shows that the Pine Island Bay branch of deep water meets the intermediate water from Thwaites Trough in the vicinity of the shear zone between the Thwaites Glacier Tongue and the Eastern Ice Shelf. In this region, warmer, saltier water of density

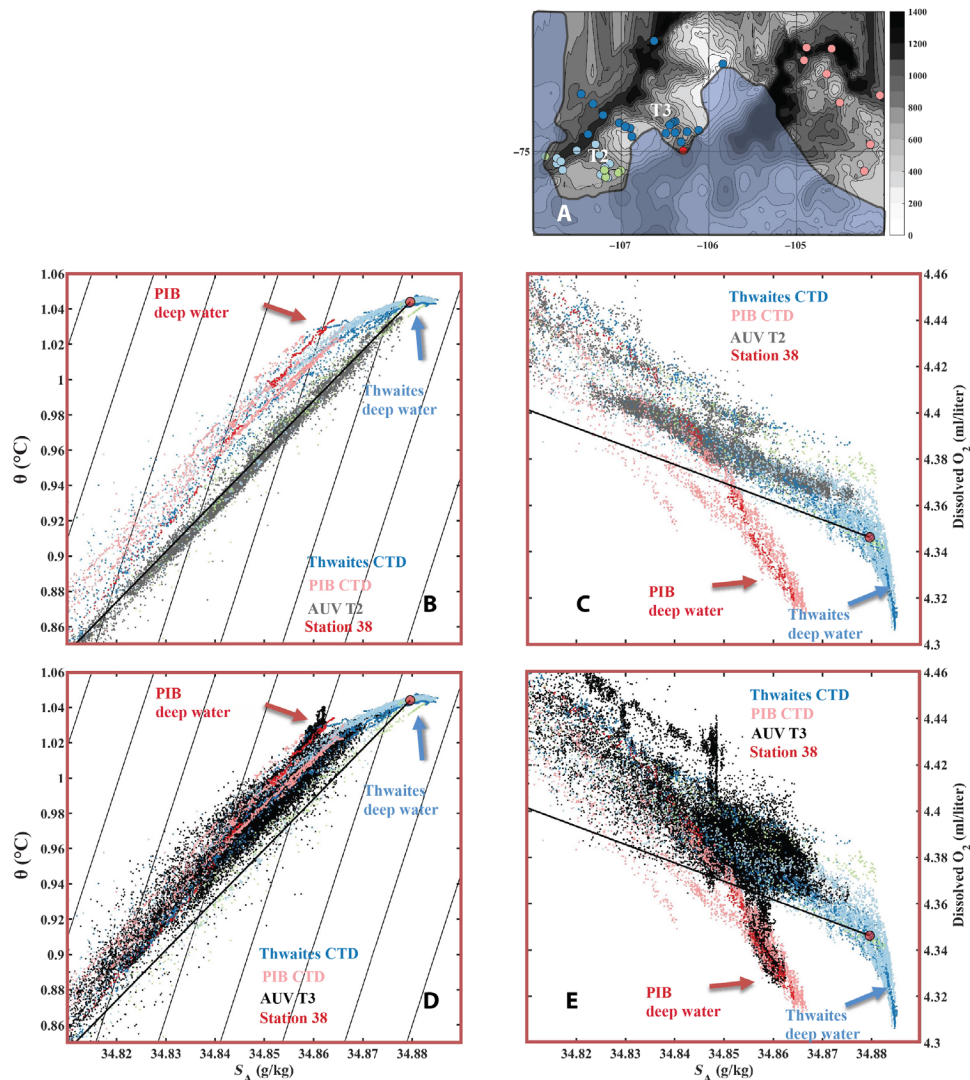


**Fig. 4. Visualization of the deep water masses in the surveyed area.** Hydrographic data obtained by CTD [colors correspond to stations in (A)]. Pine Island Bay is indicated by PIB together with data obtained by the AUV. Solid black line shows the mixing line between CDW and ice shelf melt (see Methods) (16, 18, 40). (A) Map of the region. (B) Conservative temperature  $\theta$  (in degrees Celsius) versus absolute salinity  $S_A$  (in grams per kilogram) for CTD data and AUV data from trough T2 (gray) for the zoomed parameter space indicated by red box in Fig. 3D. Solid contours show the potential density. (C) Dissolved oxygen (in milliliters per liter) versus absolute salinity  $S_A$  (in grams per kilogram) for CTD data and AUV data from trough T2 (gray) for the zoomed parameter space indicated by red box in Fig. 3E. (D) Conservative temperature  $\theta$  (in degrees Celsius) versus absolute salinity  $S_A$  (in grams per kilogram) for CTD data and AUV data from trough T3 (black) for the zoomed parameter space indicated by red box in Fig. 3D. Solid contours show the potential density. (E) Dissolved oxygen (in milliliters per liter) versus absolute salinity  $S_A$  (in grams per kilogram) for CTD data and AUV data from trough T3 (black) for the zoomed parameter space indicated by red box in Fig. 3E. Blue and red arrows indicate the two deep water types discussed in the main text.

$32.02 \text{ kg/m}^3$  meets cooler, fresher water of the same density (Fig. 5B). Those water masses can interleave and mix along isopycnals without using energy, a process that has also been recorded underneath the Ross Ice Shelf (24) where overturning and interleaving give rise to isopycnal mixing and enhanced diffusivities that can affect diapycnal heat and salt fluxes. The fact that Pine Island Bay water can still be distinguished, about 100 km from the source means that it has either only recently come into contact with the Thwaites Trough water, or there is a steady supply of water from Pine Island Bay in the east and from Thwaites Trough in the north and/or west feeding the under-ice circulation.

In contrast, the bottom water a few kilometer north of the ice-shelf front (recorded by both AUV and ship-borne CTD) was about

$0.02 \text{ g/kg}$  saltier, with temperature and dissolved oxygen similar to the Pine Island Bay deep water. This saltier type of deep water was also found underneath the ice-shelf front in trough T2 and in Thwaites Trough (Figs. 3 to 5). The fresher deep water originating in Pine Island Bay is about  $0.01 \text{ kg/m}^3$  lighter than the saltier type (Fig. 5). Since the lighter deep water is found deeper down than the denser type (800 to 1050 m compared with 700 m), there is potential for enhanced turbulence, e.g., by formation of a dense plume underneath the lighter water or through direct convection of the two water masses. It is also possible to maintain a horizontal density gradient by a vertically sheared geostrophic current (25). Hence, the region is preconditioned through the presence of the lighter water mass deep under the ice and the denser water flowing toward the

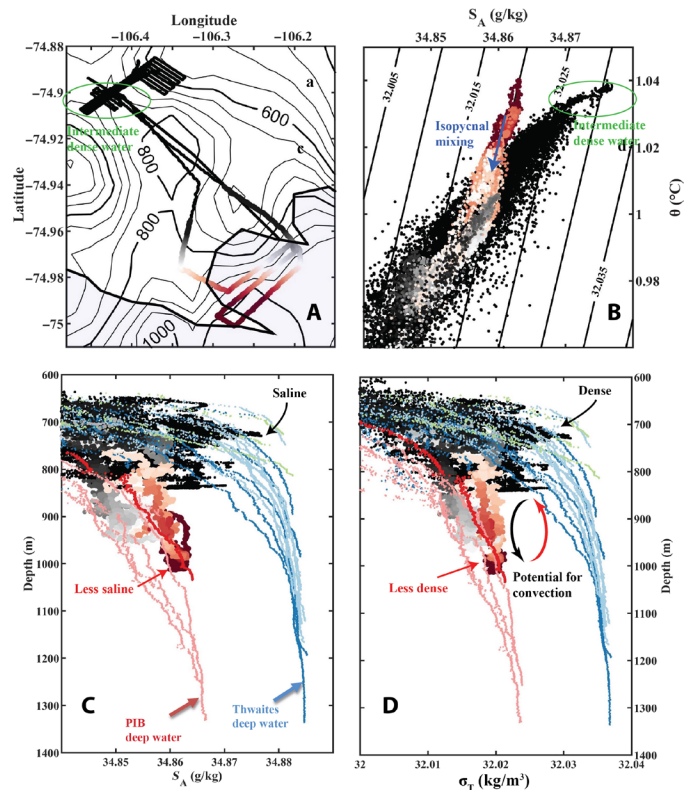


**Fig. 5. Deep water underneath the ice shelf front is lighter than water outside the ice shelf.** (A) Map of trough T3 showing the AUV path color coded by latitude. Shaded region indicates the ice shelf front, and black contours are depth contours. (B) Conservative temperature  $\theta$  (in degrees Celsius) versus absolute salinity  $S_A$  (in grams per kilogram) for the AUV data points shown in (A), colors as in (A). Contours show potential density ( $\rho$ ) relative to 900 m, and blue arrow indicates isopycnal mixing, i.e., water that has the same density but different temperatures and salinities. Green circles in (A) and (B) show the dense saline deep water found in trough T3 discussed in the main text. (C) Absolute salinity  $S_A$  (in grams per kilogram) as a function of depth for the AUV data in trough T3 and the CTD data (colors indicate station as in Fig. 3). (D) Potential density (in kilograms per cubic meter) as a function of depth for the AUV data in trough T3 and the CTD data (colors indicate station as in Figs. 3 and 4). Red and blue arrows indicate the two deep water masses discussed in the main text from Pine Island Bay and Thwaites Trough. Dissolved oxygen versus  $\theta$  and  $S_A$  is shown in fig. S6.

front, both of which are comparatively warm, for enhanced heat transport to the ice base. Our results point to the importance of further investigating the mixing processes in this region, particularly in the areas where the dense and light water masses meet.

**DISCUSSION**

We have integrated the observations presented here to define new flow paths for water moving underneath Thwaites Ice Shelf (Fig. 6) and provided the first estimate of volume and heat transport fluxes for the water derived from direct observations. We identified a meltwater-enriched outflow in the west and two distinct deep water masses that enter along different pathways, one previously unknown branch from Pine Island Bay and one directly along the Thwaites Trough, respectively. Identifying and investigating other locations where they meet are a high priority for future missions since those

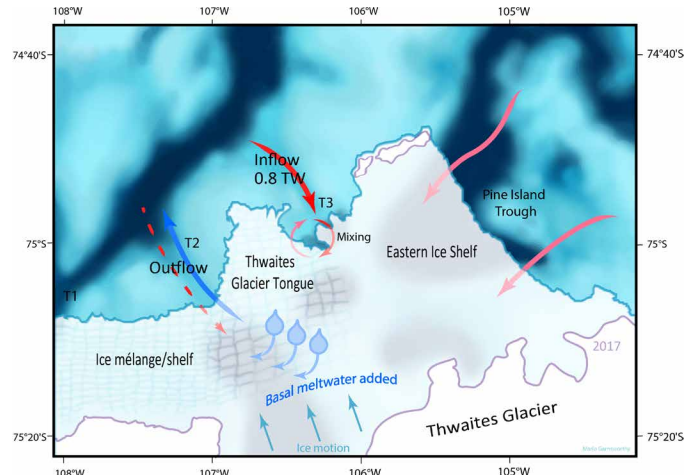


**Fig. 6. Suggested pathways and mixing area of the water underneath Thwaites ice tongue and Eastern Ice Shelf inferred from the data presented.** Red arrows indicate main pathways of warm salty water, blue arrow indicates outflow of meltwater-laden fresher water, and red dashed arrow indicates possible warm salty inflow below the range of the ship-borne ADCP. Blue shading shows bathymetric troughs, and purple lines indicate grounding zones. The two arrows from Pine Island Trough indicate that it is not possible from the present dataset to identify which part of this region sources the deep water.

locations have potential for unstable stratification and overturning, which can increase the heat flux to the ice if it occurs in contact with the ice.

The warm, salty deep water masses are entering the cavity from both sides of the pinning point at the northern tip of the Eastern Ice Shelf. The substantial heat transport in trough T3 alone is sufficient to melt ice at a rate 85 Gt/year, which is comparable to altimetry estimates (3) and model results (19) of total basal melt at the entire Thwaites Ice Shelf. This pinning point is one of the last buttressing features restraining the flow of ice from upstream, and satellite observations indicate that its extent has decreased over the past decades (26). Our observations underscore that sub-ice circulation is controlled by features in the bathymetry and ice as well as conditions at the relevant source. Since the previously unknown source of water coming from Pine Island Bay is influenced by local meteorological conditions (11) and Pine Island Glacier (27) melting, these results indicate that the future melt rate of Thwaites and ice dynamic feedbacks may depend more on local conditions in the Pine Island region, as well as the evolving ice pinning points at Thwaites (28, 29), than predicted by existing models (19, 20).

**METHODS**

**Multibeam mapping**

The bathymetry surrounding the Thwaites Ice Shelf was mapped using a 12-kHz Kongsberg EM122 multibeam echo sounder that acquires 288 bathymetric soundings per swath (with a 1° receiver). During NBP19-02, beam angles were typically between 55° and 65° (30). On survey lines that mapped from east to west immediately adjacent to the Thwaites Ice Shelf front, port beams, emitted at intermediate to high beam angles, returned an echo from the seafloor beneath the ice shelf, meaning that the sub-ice shelf seafloor was intermittently mapped inland of the ice margin. This is shown in the gridded bathymetry in Fig. 1, which extends up to 2 km beneath the ice front.

In addition, beams emitted at the widest swath angles (beam numbers typically <40) sometimes returned a strong backscatter response from the upper water column on the water column backscatter (WCB) datagram that was acquired concomitantly with the bathymetric soundings by the multibeam echo sounder. An example datagram showing the WCB anomaly (fig. S1) shows that the backscatter anomaly was subvertical and did not extend to the seafloor and the acoustic return from the seafloor on these beam angles was erroneously shallow. We interpret this backscatter anomaly as the submerged front of the floating Thwaites Ice Shelf. Therefore, by mapping this anomaly from the WCB, we were able to effectively map the face of the floating ice shelf for parts of the Thwaites margin. This is a novel use of multibeam water column data (31) and is of interest here because the base of the ice shelf along with the seafloor depth defines the water cavity thickness, which is important when investigating how warm water flows and circulates beneath the Thwaites Ice Shelf.

The floating ice-shelf face was digitized (or geo-picked) every 5 to 10 multibeam pings whenever it was visible in the WCB using QPS FMMidwater software (32). In total, the ice shelf was observed along about 58 km of the ice front (Fig. 1D). The deepest geo-pick on the datagrams was then averaged over ~3 to 5-km sections of continuously mapped ice-shelf front/face to provide an average ice-shelf depth (below sea level) for seven sections of the ice front (red stars in Fig. 1D). The mapped ice-shelf depths ranged between 180 and 495 m (below sea level) for all picks, with the deepest ice shelf occurring in the western part of the study area where the Thwaites Glacier Tongue meets the ice mélange. This is consistent with the averaged deepest ice-shelf depths, which are greatest on the south-western part of the Thwaites Glacier Tongue (Fig. 1D).

To consider errors in this method, we note that the ice-shelf face is subvertical, angling away from the centerline with increasing depth (fig. S1). If we use the datagram in fig. S1, then it is possible that the ice shelf is thicker than the 300-m depth mapped if the angle of the ice face shallows significantly at this point (i.e., becomes less steep) and is “shadowed” by the high backscatter return above. This is not consistent with our understanding of ice-shelf geometries that have gently sloping bases at their margins, on scales of hundreds of meters that we are considering here, when the ice shelf is wide and fed by high-velocity inland ice. However, if the ice shelf interacts with the bed (i.e., is partially grounded) or is made up of icebergs reconnected together by sea ice, then its thickness could be highly variable (33), and the ice-shelf face may not be indicative of the true cavity depth. For these reasons and because ice shelves thin to their margins, the ice-shelf depths reported here should be taken as minimum values and cavity thicknesses as likely maximum values. Last, we note that although airborne radar surveys also provide information about ice-shelf draft, the damaged nature of the Thwaites Glacier Tongue means that radar returns are likely to be complicated by scattering/side echo issues. The use of the WCB data during NBP19-02 provided us with an independent tool to study the ice-shelf front at the time that the oceanographic data were acquired.

### The AUV

The AUV “Ran” is a Kongsberg Hugin AUV depth rated to 3000 m. It is equipped with a Honeywell Hg9900 inertial navigation unit, aided with Nortek 500-kHz upward- and downward-looking Doppler velocity loggers (DVLs). Navigation was also aided by deploying several underwater transponders (UTPs; cNODE Maxi) at the seafloor. Using the DVL and UTP, the maximum navigation error is  $\leq 0.08\%$  of

distance traveled from the nearest UTP and was, for the two missions described here, 2 m (34). The AUV was equipped with two Sea-Bird SBE 19plus V2 systems for CTD and two Sea-Bird SBE 43 sensors for dissolved oxygen. The resolution of the sensors for temperature and conductivity is  $0.0001^\circ\text{C}$  and  $0.00005\text{ S/m}$ , producing a salinity resolution of  $0.00067\text{ g/kg}$ . The sensors were calibrated in July and August 2018 and against the ship CTD by collocating CTD casts with the AUV missions during the cruise (35). The dissolved oxygen sensor has an initial accuracy of 2% of saturation ( $0.16\text{ ml/liter}$ ), but a higher accuracy was obtained by calibration against the ship CTD.

### Ship-borne CTD

A Sea-Bird 911 CTD with dual sensor systems for conductivity, temperature, and dissolved oxygen (SBE43) was used to get depth profiles of salinity, temperature, and dissolved oxygen. Standard Sea-Bird software version Seasave V 7.26.1.8 was used for data collection and conductivity cell thermal mass correction (manufacturer recommended values were used as follows: thermal anomaly amplitude,  $\alpha = 0.03$ ; thermal anomaly time constant  $1/\beta = 7.0$ ). Salinometry measurements were made from water samples to calibrate the primary and secondary conductivity sensors on the CTD rosette (30).

### Acoustic Doppler current profiler

Two hull-mounted ADCPs, RD Instruments Ocean Surveyor models (75 and 38 kHz, respectively) were used. The data presented here are from the 38-kHz instrument, but results were cross-checked with the 75-kHz instrument (which has smaller range). The ADCP data were detided using the CATS2008 tide model (36, 37) based on the location  $75^\circ 12'\text{S}$  and  $107^\circ\text{W}$ , and the times for which the ship ADCP data were recorded (i.e., 2019-02-28 21:51:00 to 2019-03-01 01:45:00 for T2 and 2019-03-05 09:14:25 to 2019-03-06 03:36:01 for T3). The magnitude of the tides in these periods varied between 0.01 and 0.09 cm/s.

The raw data were postprocessed using the University of Hawaii Data Acquisition System software (38) and standard quality control (39) and binned in 15 min, 24-m bins. Figure S5 (A and B) shows 4-bin averages, i.e., 96-m averages, while fig. S5 (C and D) shows the 24-m binned data. The along-channel component in fig. S5 (C and D) was defined as  $41^\circ$  for T2 and  $-48^\circ$  for T3, with negative values indicating flow toward the ice shelf.

### Heat transport estimates

The heat transport  $H_F$  (in watts) toward the ice through a cross section in one of the deep troughs is given by

$$H_F = \int_{W_L}^{W_R} \int_{-D}^0 \rho C_P u (T - T_R) dz dx \quad (1)$$

where  $x$  (in meters) is the across-channel coordinate, ( $W_L$ ,  $W_R$ ) are the left and right hand boundaries of the channel,  $z$  (in meters) is the vertical coordinate,  $D(x)$  (in meters) is the seafloor,  $\rho$  ( $x, z, t$ ) (in kilograms per cubic meter) is the density,  $C_P$  (in joules per kilogram per kelvin) is the specific heat,  $u(x, z, t)$  (in meters per second) is the along-channel velocity,  $T(x, z, t)$  (in kelvin) is the temperature, and  $T_R$  (in kelvin) is the reference temperature to which the water cools after losing heat to the ice. If all available oceanic heat is used to melt ice inside the cavity, then  $T_R$  will be the in situ freezing temperature. To get an estimate of Eq. 1, the integral can be approximated by

$$H_F \approx A \bar{U} (\bar{T} - T_F) \bar{\rho} \bar{C}_P \quad (2)$$

where  $A$  is the cross-section area of the warm current,  $\bar{U}$  is the average velocity,  $\bar{T}$  is the average temperature,  $T_F \approx -2.1^\circ\text{C}$  is the freezing point at  $S_A = 34.8 \text{ g/kg}$  and a depth of 300 m (the approximate ice-shelf draft),  $\rho \approx 1025 \text{ kg/m}^3$  is the average density, and  $C_p \approx 3900 \text{ J/kg/K}$  is the average specific heat. Using a current width of 3 km (figs. S3 and S5) and a thickness of 300 m (figs. S3 and S5), the cross-section area is approximately  $0.9 \times 10^6 \text{ m}^2$ , which gives  $H_F \approx 0.9 \text{ TW}$  for channel T3 where the average velocity is approximately 0.1 m/s (fig. S5) and average temperature is approximately  $\theta \approx 0.5^\circ\text{C}$  (fig. S3). Using the same numbers, the volume flow rate is approximately 0.09 Sv. The warm layer in channel T2 is approximately 200 to 300 m in thickness, but the ADCP velocity data did not reach far enough to be able to estimate its velocity. The velocity above 500 m in depth is directed northward, but nearer the seafloor, the velocity appears to change direction, at least in the easternmost part of the trough (fig. S5C).

### Conversion to ice-melt rate

Assuming that all the energy (0.9 TW) is used for melting ice, the corresponding mass loss  $M$  (in gigaton per year) is given by

$$M = \frac{E}{L}$$

where  $E$  (in joules per second) is the heat transport and  $L$  (in joules per kilogram) is the latent heat of fusion. Using  $E = 0.9 \text{ TW}$  and  $L = 334 \text{ kJ/kg}$  gives  $M = 85.5 \text{ Gt/year}$ .

### Mixing lines

When sea water melts glacial ice, latent and direct heat is moved from the ocean (cooling the water) to the ice (warming the ice to melting temperature and melting the ice), after which the produced meltwater mixes with the ocean water. The result is a mixture that is cool (dominated by the latent heat needed to melt the ice) and fresh and has comparatively high dissolved oxygen content (as glacial ice has higher levels of dissolved oxygen than ocean water). For CDW that melts glacial ice the absolute salinity ( $S_M$ ) and dissolved oxygen content ( $O_M$ ) of the meltwater mixture is given by

$$\begin{aligned} S_M &= (1 - \alpha) S_{\text{CDW}} \\ O_M &= (1 - \alpha) O_{\text{CDW}} + \alpha O_{\text{IS}} \end{aligned} \quad (3)$$

where  $\alpha$  is the meltwater fraction,  $S_{\text{CDW}}$  and  $O_{\text{CDW}}$  are the absolute salinity and dissolved oxygen of the CDW, respectively, and  $O_{\text{IS}}$  is the dissolved oxygen of the ice-shelf meltwater. The conservative temperature ( $\Theta_M$ ) of the mixture is obtained following the thermodynamically consistent International Thermodynamic Equation of Seawater (40). The meltwater mixing lines in Figs. 3 to 6 are obtained using endpoints for CDW (red markers in Figs. 3 to 6) defined as the average of all CTD data between 800 to 1000 m in Thwaites Trough, i.e.,  $\theta_{\text{CDW}} = 1.044^\circ\text{C}$ ,  $S_{\text{CDW}} = 34.8795 \text{ g/kg}$ , and  $O_{\text{CDW}} = 4.3489 \text{ ml/liter}$ . Meltwater oxygen content was assumed to be  $O_{\text{IS}} = 30 \text{ ml/liter}$ , slightly higher than the 28 ml/liter previously used for Pine Island Glacier (17, 18), and the internal glacier temperature was assumed to be  $-15^\circ\text{C}$ , slightly lower than previously used for Pine Island Glacier (17, 18).

### Thermal wind estimates

Assuming the velocity is geostrophic, the vertical shear of horizontal velocity is given by the thermal wind equations (25)

$$\frac{\partial u}{\partial z} = -\frac{g}{f\rho_0} \frac{\partial \rho}{\partial y} \quad (4)$$

where  $u$  is the velocity in the  $x$  direction,  $g = 9.82 \text{ m/s}^2$  is the gravitational acceleration,  $f = 1.2 \times 10^{-4} \text{ s}^{-1}$  is the Coriolis parameter,  $\rho_0 = 1020 \text{ kg/m}^3$  is the reference density, and  $\frac{\partial \rho}{\partial y}$  is the horizontal derivative of density in the  $y$  direction. Using observed scales for density variations, i.e.,  $0.01 \text{ kg/m}^3$ , over a few kilometers gives scale estimate of  $\frac{\partial \rho}{\partial y} \approx 10^{-5}$  to  $10^{-6} \text{ kg/m}^4$ , or even larger. Using Eq. 4 gives geostrophic velocity shear between  $\frac{\partial u}{\partial z} \approx 10^{-3}$  and  $10^{-4} \text{ s}^{-1}$ .

### SUPPLEMENTARY MATERIALS

Supplementary material for this article is available at <http://advances.sciencemag.org/cgi/content/full/7/15/eabd7254/DC1>

### REFERENCES AND NOTES

1. P. Millilo, E. Rignot, P. Rizzoli, B. Scheuchl, J. Mouginot, J. Bueso-Bello, P. Prats-Iraola, Heterogeneous retreat and ice melt of Thwaites Glacier, West Antarctica. *Sci. Adv.* **5**, eaau3433 (2019).
2. E. Rignot, S. Jacobs, J. Mouginot, B. Scheuchl, Ice-shelf melting around antarctica. *Science* **341**, 266–270 (2013).
3. S. Adusumilli, H. A. Fricker, B. Medley, L. Padman, M. R. Siegfried, Interannual variations in meltwater input to the Southern Ocean from Antarctic ice shelves. *Nat. Geosci.* **13**, 616–620 (2020).
4. T. A. Scambos, R. E. Bell, R. B. Alley, S. Anandakrishnan, D. H. Bromwich, K. Brunt, K. Christianson, T. Creyts, S. B. Das, R. DeConto, P. Dutrieux, H. A. Fricker, D. Holland, J. MacGregor, B. Medley, J. P. Nicolas, D. Pollard, M. R. Siegfried, A. M. Smith, E. J. Steig, L. D. Trusel, D. G. Vaughan, P. L. Yager, How much, how fast?: A science review and outlook for research on the instability of Antarctica's Thwaites Glacier in the 21st century. *Glob. Planet. Change* **153**, 16–34 (2017).
5. Y. Nakayama, M. Schröder, H. H. Hellmer, From circumpolar deep water to the glacial meltwater plume on the eastern Amundsen Shelf. *Deep Sea Res. 1 Oceanogr. Res. Pap.* **77**, 50–62 (2013).
6. K. J. Heywood, L. C. Biddle, L. Boehme, P. Dutrieux, M. Fedak, A. Jenkins, R. W. Jones, J. Kaiser, H. Mallett, A. C. Naveira Garabato, I. A. Renfrew, D. Stevens, B. G. M. Webber, Between the devil and the deep blue sea: The role of the Amundsen Sea continental shelf in exchanges between ocean and ice shelves. *Oceanography* **29**, 118–129 (2016).
7. R. Millan, E. Rignot, V. Bernier, M. Morlighem, P. Dutrieux, Bathymetry of the Amundsen Sea Embayment sector of West Antarctica from Operation IceBridge gravity and other data. *Geophys. Res. Lett.* **44**, 1360–1368 (2017).
8. T. Jordan, D. Porter, K. Tinto, R. Millan, A. Muto, K. Hogan, R. Larter, A. G. Graham, J. Paden, New gravity-derived bathymetry for the Thwaites, Crosson and Dotson ice shelves revealing two ice shelf populations. *Cryosphere* **14**, 2869–2882 (2020).
9. T. J. McDougall, P. M. Barker, *Getting started with TEOS-10 and the Gibbs Seawater (GSW) Oceanographic Toolbox* (2011), pp. 28.
10. C. Moffat, M. Meredith, Shelf-ocean exchange and hydrography west of the Antarctic Peninsula: A review. *Philos. Trans. A. Math. Phys. Eng. Sci.* **376**, 20170164 (2018).
11. B. G. M. Webber, K. J. Heywood, D. P. Stevens, P. Dutrieux, E. P. Abrahamson, A. Jenkins, S. S. Jacobs, H. K. Ha, S. H. Lee, T. W. Kim, Mechanisms driving variability in the ocean forcing of Pine Island Glacier. *Nat. Commun.* **8**, 14507 (2017).
12. P. Dutrieux, J. De Rydt, A. Jenkins, P. R. Holland, K. Ha, S. H. Lee, E. J. Steig, Q. Ding, E. P. Abrahamson, M. Schroder, M. Schröder, Strong sensitivity of Pine Island ice-shelf melting to climatic variability. *Science* **343**, 174–178 (2014).
13. L. Carter, I. N. N. McCave, M. J. M. Williams, Chapter 4 circulation and water masses of the Southern Ocean: A review, in *Developments in Earth and Environmental Sciences* (Elsevier, 2008), pp. 85–114; <https://linkinghub.elsevier.com/retrieve/pii/S1571919708000049>.
14. J. E. Callahan, The structure and circulation of deep water in the Antarctic. *Deep Sea Res. Oceanog. Abstr.* **19**, 563–575 (1972).
15. C. Moffat, B. Owens, R. C. Beardsley, On the characteristics of circumpolar deep water intrusions to the west Antarctic Peninsula Continental Shelf. *J. Geophys. Res.* **114**, C05017 (2009).
16. H. G. Gade, Melting of ice in sea water: A primitive model with application to the Antarctic Ice Shelf and Icebergs. *J. Phys. Oceanogr.* **9**, 189–198 (1979).
17. A. Jenkins, The impact of melting ice on ocean waters. *J. Phys. Oceanogr.* **29**, 2370–2381 (1999).
18. L. C. Biddle, K. J. Heywood, J. Kaiser, A. Jenkins, Glacial meltwater identification in the Amundsen Sea. *J. Phys. Oceanogr.* **14**, 933–954 (2017).

19. H. Seroussi, Y. Nakayama, E. Larour, D. Menemenlis, M. Morlighem, E. Rignot, A. Khazendar, Continued retreat of Thwaites Glacier, West Antarctica, controlled by bed topography and ocean circulation. *Geophys. Res. Lett.* **44**, 6191–6199 (2017).
20. Y. Nakayama, G. Manucharyan, H. Zhang, P. Dutrieux, H. S. Torres, P. Klein, H. Seroussi, M. Schodlok, E. Rignot, D. Menemenlis, Pathways of ocean heat towards Pine Island and Thwaites grounding lines. *Sci. Rep.* **9**, 16649 (2019).
21. K. A. Hogan, R. D. Larter, A. G. C. Graham, R. Arthern, J. D. Kirkham, R. Totten Minzoni, T. A. Jordan, R. Clark, V. Fitzgerald, A. K. Wählin, J. B. Anderson, C.-D. Hillenbrand, F. O. Nitsche, L. Simkins, J. A. Smith, K. Gohl, J. E. Arndt, J. Hong, J. Wellner, Revealing the former bed of Thwaites Glacier using sea-floor bathymetry: Implications for warm-water routing and bed controls on ice flow and buttressing. *Cryosphere* **14**, 2883–2908 (2020).
22. H. K. Ha, A. K. Wählin, T. W. Kim, S. H. Lee, J. H. Lee, H. J. Lee, C. S. Hong, L. Arneborg, G. Björk, O. Kalén, Circulation and modification of warm deep water on the central Amundsen shelf. *J. Phys. Oceanogr.* **44**, 1493–1501 (2014).
23. Y. Nakayama, R. Timmermann, C. B. Rodehacke, M. Schröder, H. H. Hellmer, Modeling the spreading of glacial meltwater from the Amundsen and Bellingshausen Seas. *Geophys. Res. Lett.* **41**, 7942–7949 (2014).
24. C. Stevens, C. Hulbe, M. Brewer, C. Stewart, N. Robinson, C. Ohneiser, S. Jendersie, Ocean mixing and heat transport processes observed under the Ross Ice Shelf control its basal melting. *Proc. Natl. Acad. Sci. U.S.A.* **117**, 16799–16804 (2020).
25. B. Cushman-Roisin, J.-M. Beckers, *Introduction to Geophysical Fluid Dynamics: Physical and Numerical Aspects* (Prentice-Hall Inc., Amsterdam, The Netherlands, ed. 2, 2011).
26. E. Rignot, J. Mouginot, M. Morlighem, H. Seroussi, B. Scheuchl, Widespread, rapid grounding line retreat of Pine Island, Thwaites, Smith, and Kohler glaciers, West Antarctica, from 1992 to 2011. *Geophys. Res. Lett.* **41**, 3502–3509 (2014).
27. B. G. M. Webber, K. J. Heywood, D. P. Stevens, K. M. Assmann, B. G. M. Webber, K. J. Heywood, D. P. Stevens, K. M. Assmann, The impact of overturning and horizontal circulation in pine island trough on ice shelf melt in the eastern Amundsen Sea. *J. Phys. Oceanogr.* **49**, 63–83 (2019).
28. H. Yu, E. Rignot, H. Seroussi, M. Morlighem, Retreat of Thwaites Glacier, West Antarctica, over the next 100 years using various ice flow models, ice shelf melt scenarios and basal friction laws. *Cryosphere* **12**, 3861–3876 (2018).
29. B. W. J. Miles, C. R. Stokes, A. Jenkins, J. R. Jordan, S. S. R. Jamieson, G. H. Gudmundsson, Intermittent structural weakening and acceleration of the Thwaites Glacier Tongue between 2000 and 2018. *J. Glaciol.* **66**, 485–495 (2020).
30. R. D. Larter, B. Y. Queste, L. Boehme, S. Braddock, A. K. Wählin, A. G. C. Graham, K. A. Hogan, R. T. Minzoni, M. Barham, G. B. De Oliveira, V. F. R. Clark, S. Karam, J. D. Kirkham, A. Mazur, P. Sheehan, M. Spoth, P. Stedt, L. Welzenbach, Y. Zheng, J. Andersson, J. Rolandsson, C. Beeler, J. Goodell, E. Rush, T. Snow, “First research cruise of the International Thwaites Glacier Collaboration” (Cruise NBP19-02, International Thwaites Glacier Collaboration, 2020); [http://get.rvdata.us/cruise/NBP1902/doc/NBP1902\\_report\\_final.pdf](http://get.rvdata.us/cruise/NBP1902/doc/NBP1902_report_final.pdf).
31. K. Colbo, T. Ross, C. Brown, T. Weber, A review of oceanographic applications of water column data from multibeam echosounders. *Estuar. Coast. Shelf Sci.* **145**, 41–56 (2014).
32. L. Gee, M. Doucet, D. Parker, T. Weber, J. Beaudoin, *Hydro 12 – Taking Care of the Sea* (Hydrographic Society Benelux, 2012).
33. E. C. King, J. De Rydt, G. H. Gudmundsson, The internal structure of the Brunt Ice Shelf from ice-penetrating radar analysis and implications for ice shelf fracture. *Cryosphere* **12**, 3361–3372 (2018).
34. Ø. Hegrenæs, K. Gade, O. K. Hagen, P. E. Hagen, Underwater transponder positioning and navigation of autonomous underwater vehicles, in *Proceedings of the MTS/IEEE Oceans Conference and Exhibition* (IEEE, 2009); [www.researchgate.net/publication/224119703\\_Underwater\\_transponder\\_positioning\\_and\\_navigation\\_of\\_autonomous\\_underwater\\_vehicles](http://www.researchgate.net/publication/224119703_Underwater_transponder_positioning_and_navigation_of_autonomous_underwater_vehicles).
35. A. K. Wählin, J. Rolandsson, J. Andersson, S. Karam, A. Mazur, F. Stedt, “Ran missions from Nathaniel B. Palmer cruise NBP1902 | Swedish National Data Service” (Swedish National Data Service, 2021); <https://doi.org/10.5878/yw26-vc65>.
36. L. Padman, S. Y. Erofeeva, H. A. Fricker, H. A. Flicker, Improving Antarctic tide models by assimilation of ICESat laser altimetry over ice shelves. *Geophys. Res. Lett.* **35**, L22504 (2008).
37. S. Howard, L. Padman, S. Erofeeva, “CATS2008: Circum-Antarctic Tidal Simulation version 2008” (United States Antarctic Program Data Center, 2019); <https://doi.org/10.15784/601235>.
38. E. Firing, J. M. Hummon, *The GO-SHIP repeat hydrography manual: A collection of expert reports and guidelines - Shipboard Adcp measurements* (IOCCP Report No. 14, ICPO Publisher Serial No. 134, version 1, 2019); <http://www.go-ship.org/HydroMan.html>.
39. J. A. Taylor, A. M. Jonas, Maximising Data Return: Towards a quality control strategy for Managing and Processing TRDI ADCP Data Sets from Moored Instrumentation, in *2008 IEEE/OES 9th Working Conference on Current Measurement Technology* (IEEE, 2008), pp. 80–88; <http://ieeexplore.ieee.org/document/4480848/>.
40. T. J. Mcdougall, P. M. Barker, R. Feistel, B. K. Galton-Fenzi, Melting of ice and sea ice into seawater and frazil ice formation. *J. Phys. Oceanogr.* **44**, 1751–1775 (2014).

**Acknowledgments:** We thank J. Rolandsson and J. Andersson for essential technical assistance with the AUV operations, A. Mazur, S. Karam, and F. Stedt for assisting with the missions, the National Science Foundation Antarctic Support Contract staff for technical support, and the captain and crew on board RVIB Palmer for logistic support. **Funding:** Funding for this study has been received from the Natural Environment Research Council (grant numbers NE/S006419/1 and NE/S006664/1) and NSF, Office of Polar Programs (grant numbers 1929991 and 1738942) as part of the ITGC, from Vetenskapsrådet (2017-04257) and from the SSF project SMARC. **Author contributions:** A.K.W. was responsible for the Hugin missions, wrote the first draft, and was responsible for Figs. 2 to 5 and figs. S1 to S6. R.L. led the cruise and was responsible for commissioning Fig. 6. B.Y.Q. coordinated the physical oceanography work on the cruise. K.A.H. and A.G. coordinated collection and processing of ship-acquired multibeam echo sounding data. A.G. processed the AUV-acquired multibeam echo sounding data and was responsible for Fig. 1. K.A.H. processed the ice draft data and was responsible for Fig. 1D. L.B. coordinated the ADCP data acquisition on the cruise. J.W. contributed to the results and discussion. E.P. was principal investigator for the glacier part of the TARSAN project and contributed to the results and discussion. K.J.H. led the 2014 cruise and was principal investigator for the marine part of the TARSAN project. All authors participated in discussions on interpretation of the data and their implications. All authors commented on the paper and provided input to its final version. **Competing interests:** The authors declare that they have no competing interests. **Data and materials availability:** All data needed to evaluate the conclusions in the paper are present in the paper and/or the Supplementary Materials. All data are publicly available at the following repositories: AUV data, <https://snd.gu.se/en> (<https://doi.org/10.5878/yw26-vc65>); CTD data from the Ocean2ice iSTAR Cruise and from the 2019 NBP cruise, British Oceanographic Data Centre ([www.bodc.ac.uk](http://www.bodc.ac.uk)); CTD data from the Polarstern cruise, Pangea (<https://doi.pangaea.de/10.1594/PANGAEA.860066>); and Bathymetry data, processed multibeam echo sounding data grids with grid spacings of 50 and 500 m are available from the U.K. Polar Data Centre (<https://doi.org/10.5285/F2DFEDA9-BF44-4EF5-89A3-EE5E434A385C>). Additional data related to this paper may be requested from the authors.

Submitted 8 July 2020

Accepted 23 February 2021

Published 9 April 2021

10.1126/sciadv.abd7254

**Citation:** A.K. Wählin, A. G. C. Graham, K. A. Hogan, B. Y. Queste, L. Boehme, R. D. Larter, E. C. Pettit, J. Wellner, K. J. Heywood, Pathways and modification of warm water flowing beneath Thwaites Ice Shelf, West Antarctica. *Sci. Adv.* **7**, eabd7254 (2021).

## Pathways and modification of warm water flowing beneath Thwaites Ice Shelf, West Antarctica

A. K. Wåhlin, A. G. C. Graham, K. A. Hogan, B. Y. Queste, L. Boehme, R. D Larter, E. C. Pettit, J. Wellner and K. J. Heywood

*Sci Adv* 7 (15), eabd7254.

DOI: 10.1126/sciadv.abd7254

### ARTICLE TOOLS

<http://advances.sciencemag.org/content/7/15/eabd7254>

### SUPPLEMENTARY MATERIALS

<http://advances.sciencemag.org/content/suppl/2021/04/05/7.15.eabd7254.DC1>

### REFERENCES

This article cites 30 articles, 4 of which you can access for free  
<http://advances.sciencemag.org/content/7/15/eabd7254#BIBL>

### PERMISSIONS

<http://www.sciencemag.org/help/reprints-and-permissions>

Use of this article is subject to the [Terms of Service](#)

---

*Science Advances* (ISSN 2375-2548) is published by the American Association for the Advancement of Science, 1200 New York Avenue NW, Washington, DC 20005. The title *Science Advances* is a registered trademark of AAAS.

Copyright © 2021 The Authors, some rights reserved; exclusive licensee American Association for the Advancement of Science. No claim to original U.S. Government Works. Distributed under a Creative Commons Attribution NonCommercial License 4.0 (CC BY-NC).